

## Article

# Evaluation of Artifacts and Misinterpretation in 2D Electrical Resistivity Tomography Caused by Three-Dimensional Resistive Structures of Regular or Irregular Shapes

Raffaele Martorana \*  and Patrizia Capizzi 

Dipartimento di Scienze della Terra e del Mare, Università degli Studi di Palermo, 90123 Palermo, Italy

\* Correspondence: raffaele.martorana@unipa.it; Tel.: +39-091-238-61606

**Abstract:** Electrical resistivity tomography (ERT) is a well-known geophysical method applied to geological, hydrogeological and geoenvironmental research. To date, 2D ERT is still used much more than 3D ERT, thanks to its greater immediacy, survey speed and lower complexity in processing and inversion. However, the assumption of two-dimensionality of the underground structures can mean that the effects of 3D structures on the 2D ERT can sometimes lead to gross errors in interpretation. This work aims to evaluate these effects by testing synthetic and experimental models. Numerical simulations are performed starting from different resistivity models, and from the results, 2D data sets are derived to study and quantify the effects of 2D inversion on 3D structures. Tests simulating prismatic resistive blocks with a vertical square section are presented. Prisms extend orthogonally to the survey line. Depending on their length, they range from a minimum equal to the length of the section (cubic resistive block) to infinity (2D prism). On these models, 2D and 3D electrical resistivity tomography (ERT) surveys are simulated. The results show that resistive blocks with a limited extension orthogonal to the profile are not effectively resolved by 2D ERT. Additionally, resistivity values obtained from a 2D ERT inversion on a 3D resistive prism are underestimated more than those obtained on the corresponding 2D prism when compared with the true value. This underestimation increases with the three-dimensional characteristics. Furthermore, resistive blocks located near the survey line but not crossed by it create artifacts that can lead to erroneous interpretations. A field test performed on a calcarenite quarry, of which the three-dimensional geophysical model was reconstructed, confirmed the results obtained by the synthetic tests, highlighting that the effects of three-dimensionality can lead to the identification of artifacts in the vertical section or produce strong errors in the estimation of depth and size, thus causing misleading statements.

**Keywords:** applied geophysics; electrical resistivity tomography; 3D structures; artifacts; cavity; inversion



**Citation:** Martorana, R.; Capizzi, P. Evaluation of Artifacts and Misinterpretation in 2D Electrical Resistivity Tomography Caused by Three-Dimensional Resistive Structures of Regular or Irregular Shapes. *Appl. Sci.* **2023**, *13*, 2015. <https://doi.org/10.3390/app13032015>

Academic Editors: Daniele Sampietro, Martina Capponi and Lydie Sarah Gailler

Received: 4 January 2023

Revised: 30 January 2023

Accepted: 1 February 2023

Published: 3 February 2023



**Copyright:** © 2023 by the authors. Licensee MDPI, Basel, Switzerland. This article is an open access article distributed under the terms and conditions of the Creative Commons Attribution (CC BY) license (<https://creativecommons.org/licenses/by/4.0/>).

## 1. Introduction

Today, electrical resistivity tomography (ERT) is a widely used method in many geological and environmental applications [1]. It is often preferred to opt for 2D arrays because they are easier and quicker to carry on compared with 3D arrays, especially in urban environments. The latter requires not only the dense data coverage to be significant, therefore having a higher acquisition cost, but also a consequent use of more memory and powerful computers. This problem, however, is less important today than in the past, thanks to the development of multi-channel data acquisition systems. In fact, for the optimal exploitation of these characteristics, new and different arrays and acquisition methods have been proposed for surveys that involve thousands of electrode positions [2–8], as well as the use of more powerful computers and better-performing software [6,9].

When heterogeneity is present, three-dimensional imaging of 2D electrical resistivity data sets should provide a more accurate and reliable picture of the subsurface than single analyzed 2D ERTs [10] and generally increases the resolution of the resistivity survey [11].

Another effective data acquisition strategy for 3D sensing is to combine perpendicular 2D slices and interpret them together [11–14].

Unfortunately, 2D electrical resistivity tomographies are sufficient to derive realistic subsurface models only when the subsoil is geologically quite simple [15]. Conversely, when in the presence of structures that cannot be simplified as 2D with respect to the survey line, such as complex geological structures or anthropogenic structures such as building foundations or underground cavities, 2D surveys can produce misleading models due to the three-dimensional nature of these structures [16,17]. Indeed, the 2D ERT inversion algorithms assume that the electrical resistivity does not change in the direction perpendicular to the ERT profile. When the subsoil does not respect this assumption, they generate 3D effects [18,19] which should be quantified or at least recognized in 2D inversions.

While the effects of 2D structures on 1D resistivity modeling have been studied [20], the effects of three-dimensional structures on 2D ERT are less understood [21,22].

Recently, some studies have been conducted on the topographical effects of embankment structures located next to 2D apparent resistivity pseudosections [23–26]. However, little information is available on the deformations of the 2D ERTs caused by underground three-dimensional structures crossing the tomographic section or coming close to it [27,28]. In this regard, Hung et al. [29] investigated the boundary effects on 2D ERT by varying some potential factors, such as the resistivity contrast, depth and size of buried objects and electrode spacing.

This work aims to study the effects on the 2D ERT inversion of three-dimensional structures present below or near the survey line using data derived from synthetic models and field measurements. For this purpose, several numerical simulations have been performed on resistivity models with resistive blocks of a regular shape, and some parameters have been calculated to quantify the 3D effects on the inversion reliability. Furthermore, based on a detailed speleological study carried out on a quarry, a complex three-dimensional model of the quarry was simulated. The results were considered and compared with the field results for the same quarry.

## 2. Materials and Methods

### 2.1. Basic Electrical Resistivity Tomography, Forward Modeling and Inversion

Electrical resistivity techniques allow for estimating the distribution of the electrical resistivity of the subsoil. They are essentially based on Ohm's two laws, from which we can derive the following equation in vector form for the current flow in a continuous medium:

$$\mathbf{J} = \sigma \nabla \Phi, \quad (1)$$

where  $\mathbf{J}$  is the current density,  $\Phi$  is the electric field potential and  $\sigma$  is the conductivity of the medium, which is equal to the reciprocal of the resistivity  $\rho$ .

Equation (1) describes the relationships between the potential of the electric field generated by an electromotive force, the current flowing through the ground and the resistance of the subsoil. The latter depends on the distribution of the electrical resistivity in the subsoil and on the positions of the electrodes. To perform a resistivity measurement, an electric current  $I$  is generated in the ground by applying an electromotive force through two current electrodes. The trend of the electric field is observed by measuring the potential differences  $\Delta V$  with electrodes appropriately arranged on the surface. Considering the subsoil as a homogeneous half-space, the apparent resistivity  $\rho_a$  is calculated by the following formula [30]:

$$\rho_a = k \Delta V / I, \quad (2)$$

where  $k$  is a geometric factor which depends on the positions and shapes of the electrodes.

Over the years, different electrode arrays have been conceived and used for resistivity surveys, each having different characteristics and being suitable for different modeling (1D, 2D or 3D). The advantages and disadvantages of each of these arrays depend on many factors, including the sensitivity, signal-to-noise ratio, depth of investigation [31,32]

and lateral coverage [33]. Recently, the use of multichannel systems has allowed connecting up to several hundreds of electrodes at once, greatly reducing the survey time. This feature has led to the need to choose arrays that allow the contemporary voltage measurements of many potential dipoles for each current dipole, such as the Wenner–Schlumberger or linear dipole-dipole arrays. Furthermore, optimized arrays for multi-channel acquisitions have been proposed [2–5,7].

The forward problem of calculating the electric potential due to a point source located in  $(x_s, y_s, z_s)$  consists of the solution of the following equation [34]:

$$\nabla \left[ \frac{1}{\rho(x, y, z)} \nabla \Phi(x, y, z) \right] = -\frac{\partial j_c}{\partial t} \delta(x - x_s) \delta(y - y_s) \delta(z - z_s), \quad (3)$$

where  $\rho$  is the electrical resistivity at the coordinate point  $(x, y, z)$ ,  $\Phi$  is the potential at the same point,  $j_c$  is the electrical charge density and  $\delta$  is the Dirac delta function.

Generally, forward modeling uses approximate approaches through finite difference [34–36] or finite element [37] methods in which the subsurface is represented by a grid of meshes, inside which the electrical resistivity is constant or varies linearly.

In ERT, the inverse problem is not linear and ill-posed, and it is generally faced by solving the forward problem iteratively, starting from a simple initial model  $m_0$  (usually a homogeneous half-space) and minimizing the misfit between the measured and calculated data. The most common approach applies, with appropriate modifications, the damped least squares method [38] based on the following equation [39–41]:

$$(\mathbf{J}^T \mathbf{J} + \lambda \mathbf{I}) \Delta \mathbf{q} = \mathbf{J}^T \Delta \mathbf{g}, \quad (4)$$

where  $\Delta \mathbf{g}$  is the vector of the difference between the logarithms of the observed and calculated apparent resistivities,  $\Delta \mathbf{q}$  is the vector of the difference between the logarithm of the resistivity of each mesh of the  $k + 1^{th}$  model and the same parameters of the  $k^{th}$  model,  $\mathbf{J}$  is the Jacobian matrix of the partial derivatives of the apparent resistivities with respect to the model parameters,  $\lambda$  is a damping factor and  $\mathbf{I}$  is the identity matrix.

When the number of parameters is too large, the damped least squares method tends to be unstable [42]. The issues of poor posing and poor constraint of the inverse problem can be addressed in different ways. If the subsurface resistivity is expected to change smoothly, then the algorithm is modified by introducing smoothness constraints directly on the model resistivity values. The resulting smoothness-constrained least squares method [43,44] has the following mathematical form:

$$(\mathbf{J}^T \mathbf{J} + \lambda \mathbf{F}) \Delta \mathbf{q} = \mathbf{J}^T \Delta \mathbf{g} - \lambda \mathbf{F} \mathbf{q}, \quad (5)$$

where  $\mathbf{F}$  is a linear combination of roughness filter matrices.

In the case in which the subsoil structures can be represented by homogeneous zones separated by sharp boundaries, an  $L_1$ -norm criterion can be used to produce “blocky” models [45,46]. The optimization equation in Equation (5) is modified to

$$(\mathbf{J}^T \mathbf{R}_d \mathbf{J} + \lambda \mathbf{F}) \Delta \mathbf{q} = \mathbf{J}^T \mathbf{R}_d \Delta \mathbf{g} - \lambda \mathbf{F} \mathbf{q}, \quad (6)$$

where  $\mathbf{R}_d$  and  $\mathbf{F}_R$  are weighting matrices (see [46] for further details). The latter, also called the blocky method or robust method, tends to resolve models in which the resistivity is constant piecewise [43].

## 2.2. Design of Synthetic Models

The design of synthetic models was based on simplicity criteria aimed at quantitative evaluation of the interpretative distortions that can arise when three-dimensional structures are investigated with two-dimensional resistivity surveys. The two-dimensional approach inevitably leads to an incorrect estimate of the size and electrical resistivity of the anomalous zone. It was therefore decided in the first phase to simulate resistive blocks

of simple and regular shapes to obtain inverse models that would allow a quantitative parametric approach and a systematic comparison between 3D resistivity models and the corresponding 2D inverse models when 2D-ERT surveys were simulated.

For the 3D forward modeling, RES3DMOD software was used [47], considering the finite element method and a grid of rectangular meshes in which  $48 \times 21$  electrodes spaced at 2 m in the  $x$  and  $y$  directions, respectively, were considered. For each designed model, the apparent resistivity measurements related to a 3D data set were calculated. The 3D electrical resistivity survey was simulated while considering the inline dipole-dipole array, with the dipole length  $a$  ranging from 1 to 12 times the electrode spacing and the dipole-dipole distance  $n$  ranging from 1 to 12 times the electrode spacing. This array configuration allows a good resolution and reliability for the survey according to a not-too-long acquisition time [7,48,49]. The dipole-dipole array allows, thanks to modern multi-channel instruments, simultaneously acquiring many voltage measures with the same current dipole input, thus allowing short acquisition times and, consequently, a large number of measures which are difficult to acquire in reasonable times using Wenner or Wenner–Schlumberger arrays.

From these data sets, some parallel 2D data sets related to the parallel profiles were extracted and separately inverted to study and quantify the effects of 3D structures on 2D inversion, parametrically estimating the differences between 2D imaging and the corresponding section of the 3D inverse model.

The first and simplest model considered was a resistive cube ( $10^5 \Omega \cdot \text{m}$ ) centered under the grid of a size  $l = 8 \text{ m}$  in a background rock of  $100 \Omega \cdot \text{m}$  (Figure 1). The depth of the upper face of the cube was  $h = 4 \text{ m}$ . From the obtained 3D data set of calculated apparent resistivities, some 2D data subsets were extracted, simulating many parallel 2D surveys along the  $x$  direction placed at variable distance  $d$  between the center of the survey line and the projection on the surface of the center of the cube.

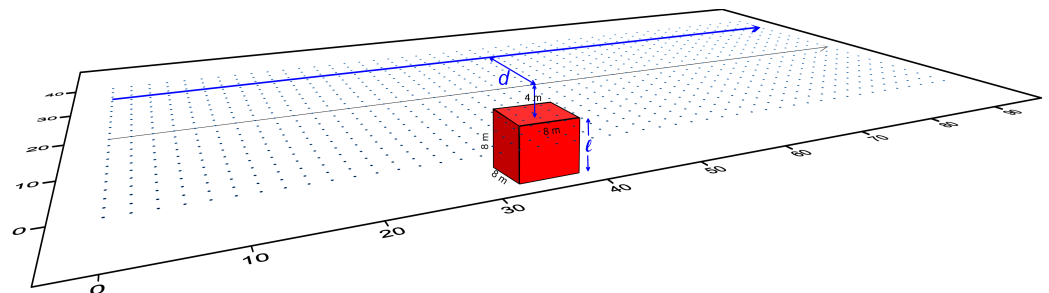


**Figure 1.** Simulation of a 3D ERT survey on a model of a cube-shaped resistive block ( $10^5 \Omega \cdot \text{m}$ ) buried in a background rock ( $100 \Omega \cdot \text{m}$ ). The blue points indicate the electrode positions. The size  $l$  of the cube is equal to 8 m. The depth of the top of the cube is 4 m. The thick blue line indicates the considered 2D-ERT survey, carried out at an orthogonal distance  $d$  from the projection on the surface of the cube's center.

The second test (Figure 2) regarded a series of prism-shaped cavities with a square vertical section of a size  $l = 8 \text{ m}$  and a length in the orthogonal  $y$  direction that ranged from  $s = 8 \text{ m}$  (the same as the first model) to  $s \rightarrow \infty$ , the latter being a 2D tunnel model of the squared section (Figure 3) simulated with the RES2DMOD software [50]. In these cases, the 3D electrical resistivity surveys were simulated while considering the same electrode arrays and measurement sequences as those in the previous case. From each of these 3D data sets, a 2D subset was extracted, simulating a survey that passed over the center of the cavity and crossed it perpendicular to its width  $s$  ( $x$  direction).

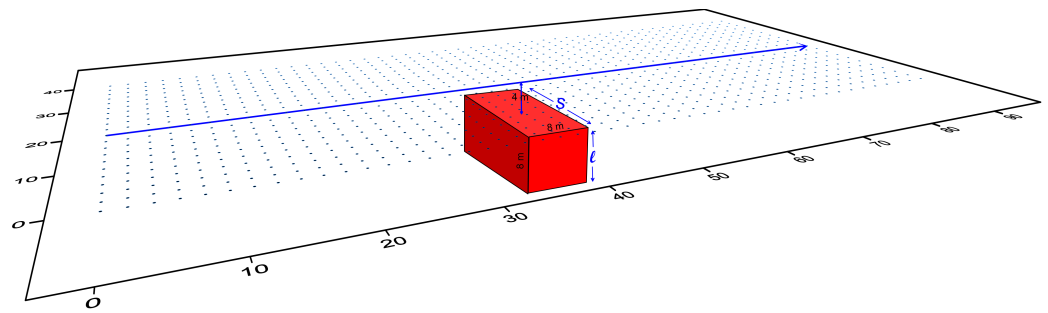


**Figure 2.** Simulation of a 3D ERT survey on a model of a prism-shaped resistive block ( $10^5 \Omega\cdot\text{m}$ ) with the orthogonal width  $s$  not equal to the longitudinal and vertical sizes  $l$  in a background rock ( $100 \Omega\cdot\text{m}$ ). The size  $l$  of the square section is equal to 8 m. The depth of the top of the prism is 4 m. The thick blue line indicates the considered 2D ERT survey carried out over the prism center in the orthogonal direction to the length  $s$  of the prism.

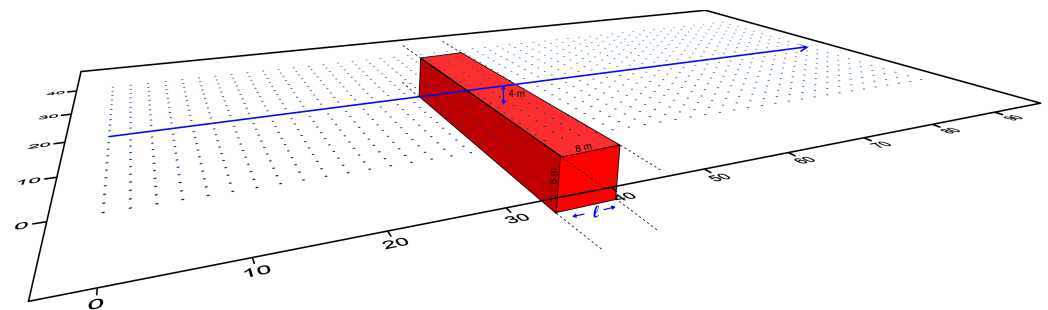


**Figure 3.** Simulation of a 2D ERT survey ( $10^5 \Omega\cdot\text{m}$ ) in a background rock ( $100 \Omega\cdot\text{m}$ ).

### 2.3. Parameters to Estimate the Inversion Reliability

The inversion of the calculated data was performed using the RES2DINVx64 [51] and RES3DINVx64 [52] programs. To perform a quantitative comparison, the inversion parameters were set to be the same for all the inversions made so that the results could be correctly compared and discussed. An  $L_1$ -norm robust model inversion constraint [46] was used to obtain models capable of highlighting sharp boundaries with a high resistivity contrast. This is the most appropriate method for delineating the shape of the anomalous block. In this case, the discrepancy between the predicted and observed data was expressed as the absolute error through the  $L_1$ -norm normalized data misfit  $L_{1N}$ . We set a convergence limit for the relative change in the  $L_{1N}$  misfit equal to 2% and a maximum number of iterations for the inversion equal to 10. For all simulations, the mesh sizes were chosen to be equal to half the electrode distance for both the forward problem and the inverse problem to take into account the abrupt resistivity changes of the models.

The evaluation of the results had to include a quantitative analysis of the defined parameters indicating the ability of the inverse model to approach the real situation. Therefore, to evaluate the overall effectiveness of each inversion, some simple comparison parameters were considered.

The first parameter is given by

$$P_1 = \frac{\rho_{prism}(l, s, d)}{\rho_{prism}(l, \infty)}, \quad (7)$$

where  $\rho_{prism}(l, s, d)$  is the average value of the electrical resistivity calculated in the area of the anomaly (the one in which the resistivity exceeded the background one by 15% was considered),  $l$  is the square section size of the prism,  $s$  is its orthogonal size,  $d$  is the orthogonal distance from the center of the prism at which the survey is carried out and  $\rho_{prism}(l, \infty)$  is the corresponding value when  $s \rightarrow \infty$  (tunnel model shown in Figure 3).

Basically,  $P_1$  gives the ratio between the resistivity anomaly caused by a 3D block with a given vertical section and a given electrical resistivity and that caused by a 2D prism with the same vertical section and resistivity. Consequently, this reflects how much the three-dimensionality affects the electrical resistivity value of the anomaly obtained from a 2D inversion, decreasing the estimate. To calculate the anomalous area, the threshold of 15% was chosen following some tests to exclude small variations in resistivity in the section, which may have been caused by noise or inaccuracy of the inversion.

The second parameter is given by

$$P_2 = \frac{\rho_{prism}(l, s, d)}{\rho_{prism}(l, 0)}, \quad (8)$$

where the section centered on the prism is considered for the denominator ( $d = 0$ ) and  $P_2$  indicates how much the non-centrality of the 2D ERT with respect to the resistive block affects the inversion. It was calculated only for the model of the cubic resistive block.

The third parameter considered is defined as

$$P_3 = \frac{\sum_{anom}(l, s, d)}{\sum_{prism}(l, s, d)}, \quad (9)$$

where  $\sum_{anom}(l, s, d)$  is the area of the resistive anomaly (in which the resistivity exceeds the background one by 15%) as shown by the inverse model and  $\sum_{prism}(l, s, d)$  is the actual area of the prism section.  $P_3$ , therefore, shows the percentage of the anomalous area detected with respect to the real one.

### 3. Results: Discussion and Comparison

The discussion of the results first follows a qualitative approach, comparing the obtained inverse models with each other and with the synthetic model, and subsequently a quantitative approach, calculating the inversion reliability parameters previously described.

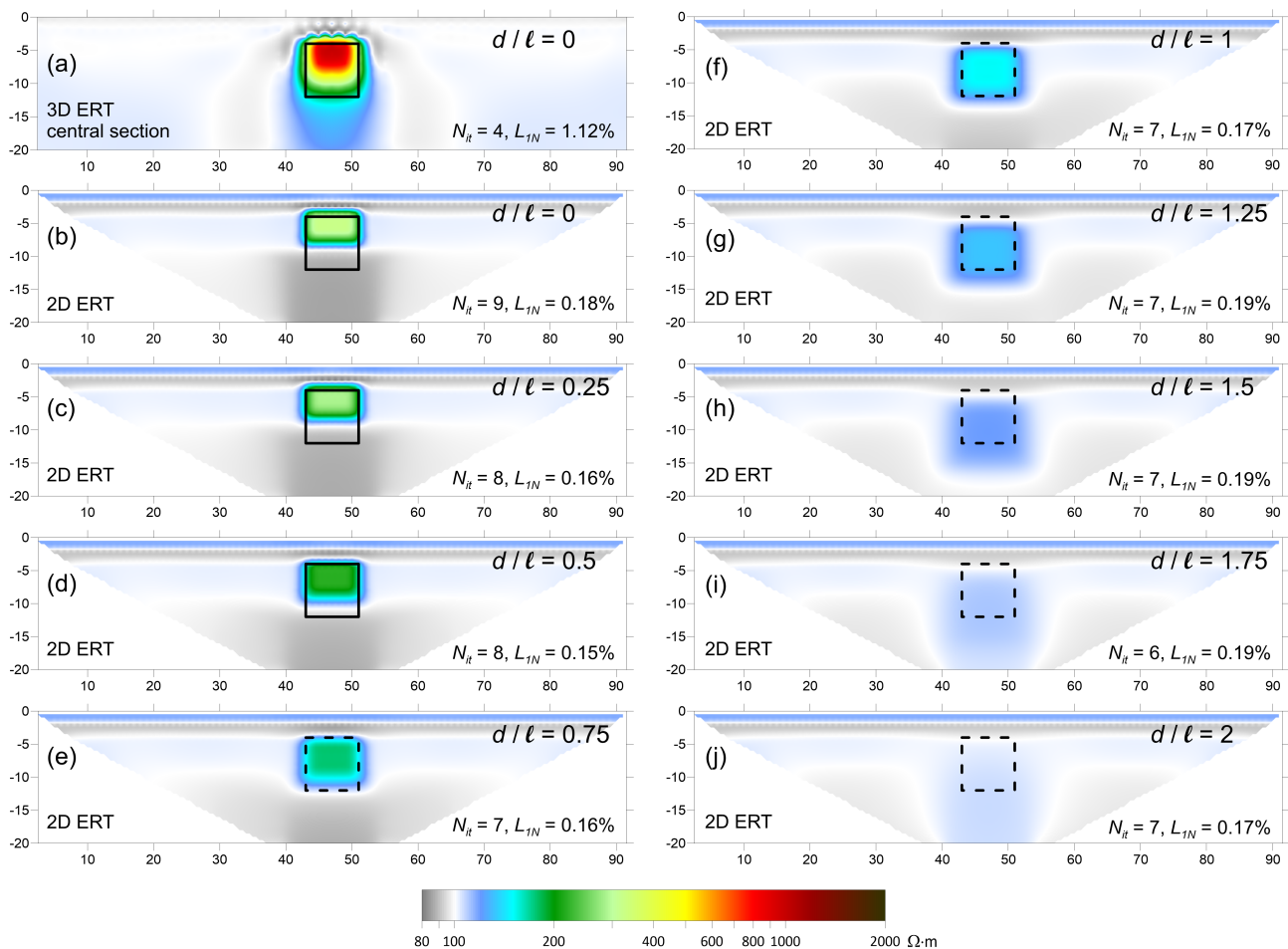
All the electrical resistivity sections are presented with the same logarithmic scale of colors to facilitate comparison. This is highlight, with a rainbow scale, only the resistivity values greater than the background resistivity (100  $\Omega \cdot m$ ). The smaller values instead were rendered with shades of gray.

Figure 4 summarizes the inverse models obtained starting from the cube model (see Figure 1). The 2D ERT surveys are related to electrode lines arranged at different values of the orthogonal distance  $d$  between the survey line and the projection on the surface of the center of the cube (Figure 4b–j). The results can be compared with the central section ( $d/l = 0$ ) extracted from the 3D ERT inverse model (Figure 4a) in which the number of iterations  $N_{it} = 4$  and the normalized data misfit  $L_{1N} = 1.12\%$ .

In 2D inversions, a greater number of iterations than for 3D inversions is necessary for the process to stop ( $N_{it}$  ranging from 6 to 9), obtaining very low data misfit values ( $0.15\% \leq L_{1N} \leq 0.19\%$ ). However, a low data misfit value does not indicate good results. In fact, the 2D ERT results showed strong variations in the shape of the anomaly compared with the true one. When the 2D survey was centered upon the cube, the height of the anomaly was strongly underestimated, resulting in about half of the real height of the cube. On the other hand, the width was determined with good precision (Figure 4b). When the 2D survey was performed lateral to the cube, the height of the anomaly increased, but its width increased compared with the real one as  $d$  increased (Figure 4c–j). As expected, the displayed resistivity value of the anomaly was always less than that of the cube.

However, while in the case of the central section of the 3D ERT the maximum resistivity value was quite high (about 1000  $\Omega \cdot m$ , Figure 4a), in the 2D ERT, it was much lower, varying from about 320  $\Omega \cdot m$  when  $d/l = 0$  (Figure 4b) down to 106  $\Omega \cdot m$  when  $d/l = 2$  (Figure 4j).

Anyway, the effects of the resistive cube were still quite evident even if the 2D survey no longer passed over the cube, or at least for non-excessive distances ( $0.5 < d/l < 1.5$ , Figure 4e–h). This generates a misleading anomaly that can lead to errors in interpretation.



**Figure 4.** Inverse models obtained starting from the 3D model of cube-shaped resistive block. (a) Central section of the 3D ERT and (b–j) 2D ERT when varying the orthogonal distance  $d$  between the electrode line and the projection in the surface of the center of the cube. The solid black line indicates the boundaries of the cube when the section intersects it. The dashed black line indicates the projection of the boundaries of the cube when it is not intersected by the section.

The effectiveness parameters  $P_1$ ,  $P_2$  and  $P_3$ , previously defined to quantify the effectiveness of 2D inversions with respect to the real section, were calculated for each simulated 2D ERT. The results are shown graphically in Figure 5 for the cube-shaped resistive block model. The value of  $P_1$  was always very low ( $P_1 < 0.15$ ) and decreased as  $d/l$  increased, confirming the strong underestimation of the 3D anomaly when this was interpreted as 2D. The parameter  $P_2$ , which quantifies the effect of the non-centrality of the 2D ERT with respect to the resistive block, decreased from 1 to about 0.5 when  $d/l$  increased from 0 to 2.5. The parameter  $P_3$  is related to the amount of anomalous area detected with respect to the real one. This parameter surprisingly indicated that the extension of the anomalous structure was underestimated when the distance  $d$  was less than half the dimension  $l$  of the cube. It increased as  $d/l$  increased until  $d/l$  reached 1.25 and then decreased, tending toward zero for  $d/l > 2$ .

In short, the simulations relating to the model in Figure 1 show how the influence on the inversion of a resistive block depends on its position with respect to the survey line. As the distance between the resistive block and the survey line increased, the resistivity contrast decreased, while the extent of the anomaly initially increased and then decreased as well.

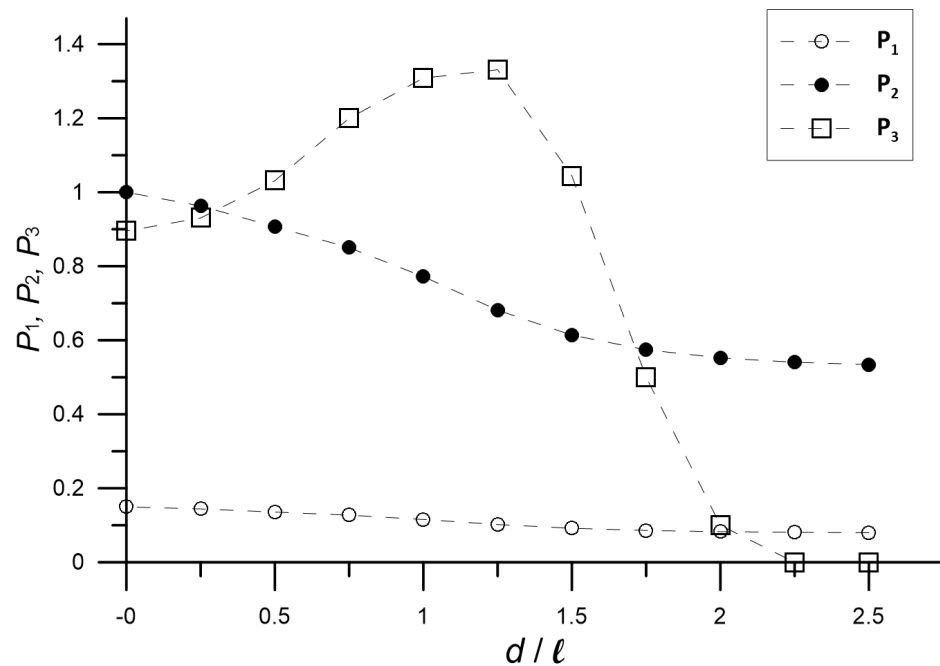


**Figure 5.** Trend of the inversion effectiveness parameters  $P_1$ ,  $P_2$  and  $P_3$ , referring to the cube-shaped model shown in Figure 1, as the ratio  $d/l$  between the orthogonal distance  $d$  and the side of the cube  $l$  increases.

Figure 6 summarizes the 2D inverse models obtained starting from the 3D prism-shaped models (see Figure 2). For these simulations, it was considered that the electrode lines always passed above the center of the prism perpendicular to its axis. Therefore, the orthogonal distance  $d$  between the electrode line and the projection on the surface of the center of the cube was always equal to zero, instead varying the orthogonal width  $s$  of the prism.

The number of iterations needed to stop the inversion was comparable to the previous case ( $N_{it}$  ranged from 6 to 10), while the data misfit was slightly higher ( $0.16\% \leq L_{1N} \leq 0.26\%$ ). Additionally, for these inversions, there was no correlation between the low misfit values and the likelihood of the inverse models.

The shape and value of the anomaly were close to those of the corresponding 2D model (Figure 6a) when the ratio  $s/l > 4$  (Figure 6b–d). For prisms with  $s/l < 3$ , the prism was still identifiable, but its size and resistivity were progressively underestimated as  $s$  decreased.

For the same prism-shaped models, the central sections extracted from the 3D ERT inverse models are reported in Figure 7. In all these sections,  $d = 0$  while the orthogonal length  $s$  of the prism varied from 0 to 5 times the side  $l$  of the square vertical section.

In the 3D inversions, the number of iterations  $N_{it}$  ranged from 5 to 9, while the  $L_1$ -norm data misfit ranged from 0.07% to 0.20% and was generally less than that in the respective 2D inversions. For all models of prisms in which  $s > l$  (Figure 7b–i), the central sections of the inverse 3D models showed the shape of the anomaly that closely approximated the square section of the prism. The resistivity values of the anomalies, while continuing to be significantly lower than those of the model, were only slightly lower than those shown by the 2D ERT (Figure 7a). When  $s \rightarrow l$ , the anomaly was flattened, and its resistivity was significantly lower (Figure 7j).

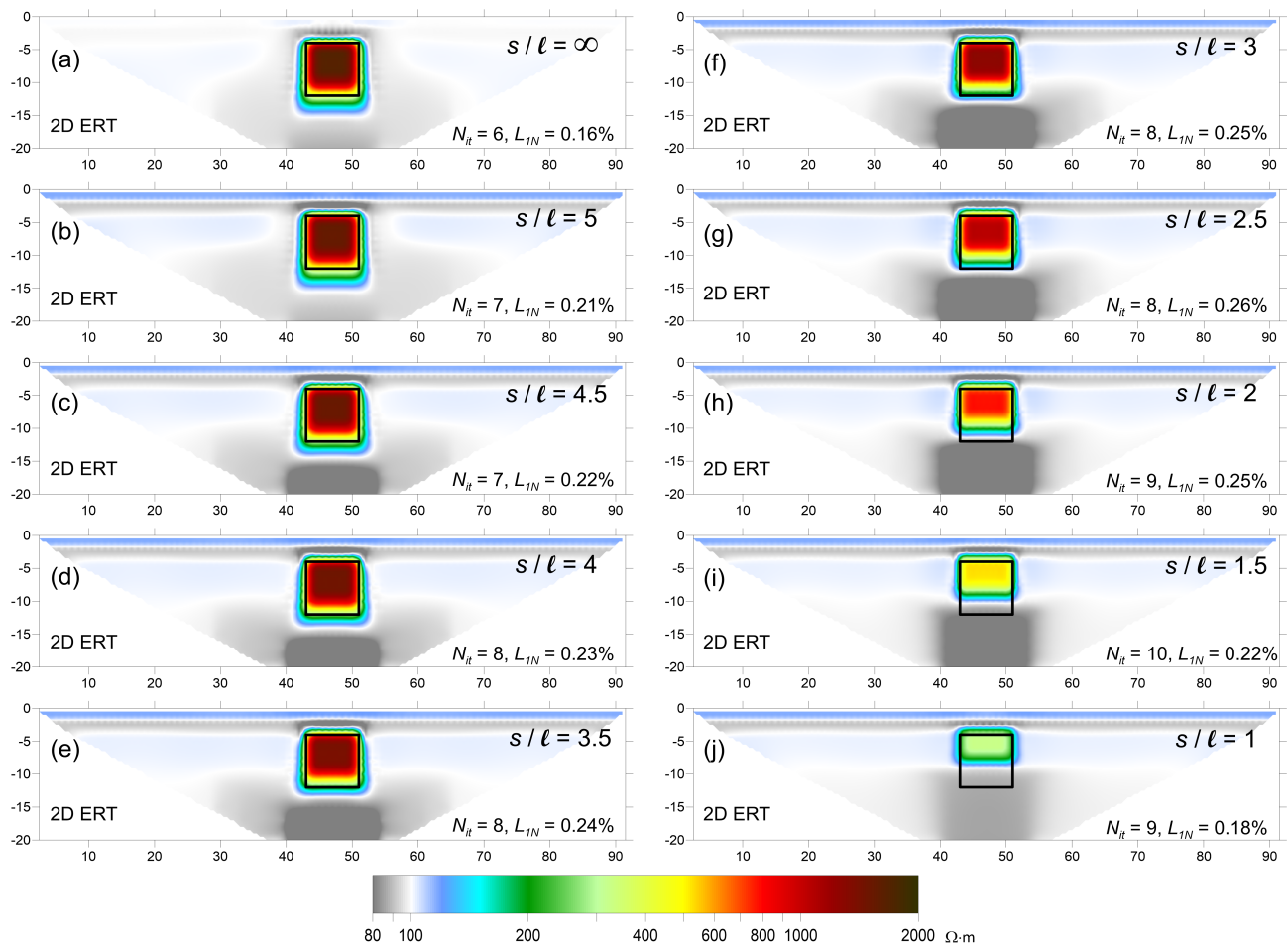


**Figure 6.** 2D ERT inverse models obtained starting from the 3D models of prism-shaped resistive blocks, with different values for the orthogonal width  $s$  of the prism, where (a)  $s/l = \infty$  (2D model) and (b–j) from  $s/l = 5$  to  $s/l = 1$  (cube model). The orthogonal distance  $d$  between the electrode line and the projection on the surface of the center of the cube was equal to zero for all the inversions. The solid black line indicates the boundaries of the prism.

Figure 8 summarizes the trends of parameters  $P_1$  and  $P_3$ , calculated for the results obtained from the models shown in Figures 2 and 3. Considering the 2D ERT of Figure 6 centered over the prism,  $P_1$  (white circles) increased as  $s/l$  increased, approaching 1 when  $s/l \geq 5$ . It follows that, considering the returned resistivity value, a prismatic structure could be considered comparable to a two-dimensional structure when the ratio between the length of the prism and the side of its section was at least equal to five. Parameter  $P_3$  (white squares) followed the same trend as  $P_1$ , albeit while showing higher values, and in any case greater than one, except when the prism approached the dimensionality of a cube. For all other values, the anomalous area was always overestimated, and this overestimation increased with the perpendicular length  $s$ .

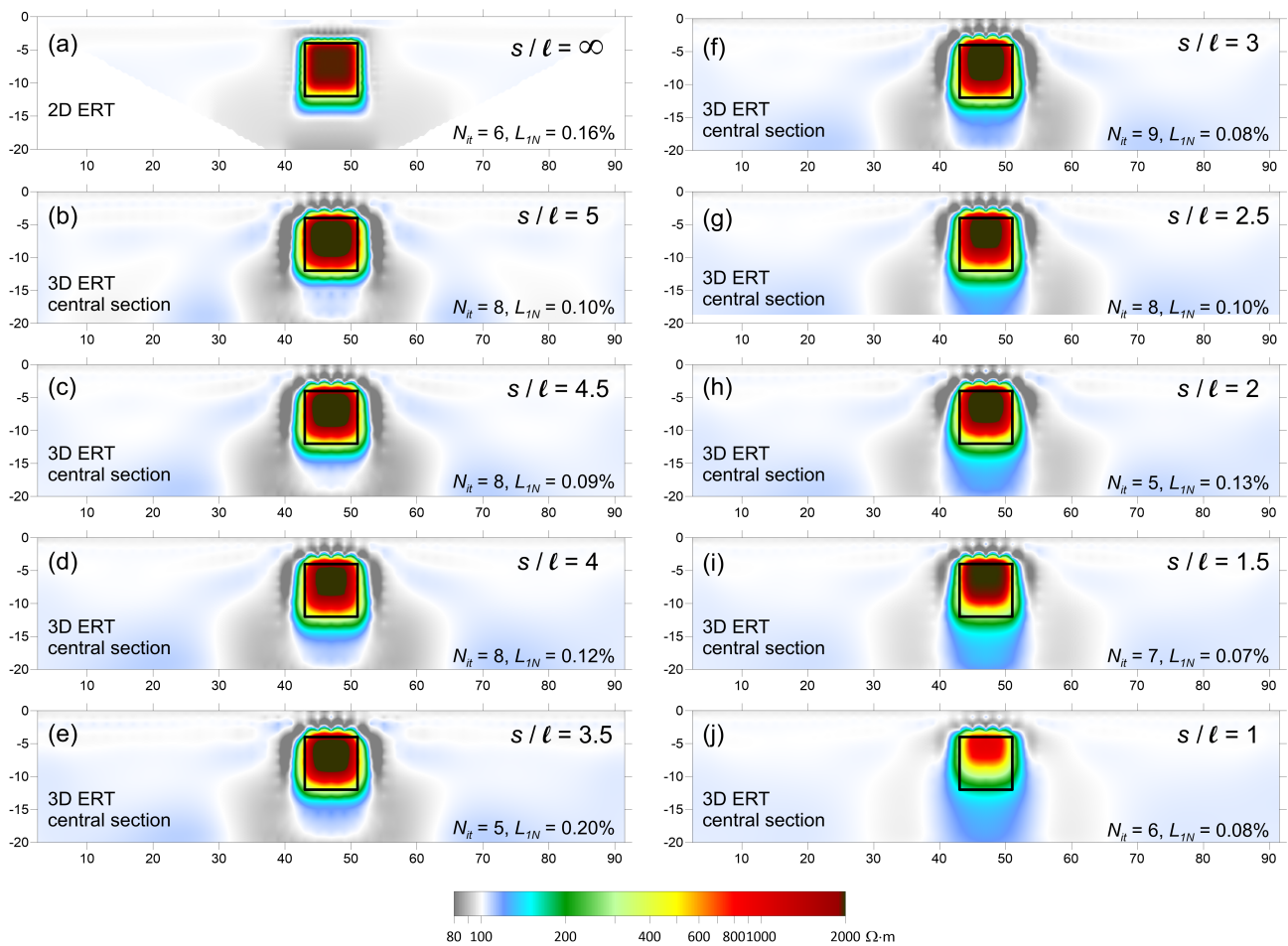


**Figure 7.** Central sections ( $d = 0$ ) extracted from 3D ERT inverse models obtained starting from the 3D models of prism-shaped resistive blocks. (a)  $s/l = \infty$  (2D model) and (b–j) from  $s/l = 5$  to  $s/l = 1$  (cube model). The orthogonal distance  $d$  between the section and the projection on the surface of the center of the cube was equal to zero for all the sections. The solid black line indicates the boundaries of the prism.

Instead, considering the central sections of the 3D ERT in Figure 7,  $P_1$  (black circles) increased irregularly as  $s/l$  increased, approaching 1 when  $s/l \geq 5$ . It follows that, considering the returned resistivity value, a prismatic structure could be considered comparable to a two-dimensional structure when the ratio between the length of the prism and the side of its section was at least equal to five.  $P_3$  (black squares) showed the opposite trend to  $P_1$ , indicating that the overestimation of the anomalous area decreased as the perpendicular dimension  $s$  increased, tending to double the real section when  $s$  tended toward infinity.

The test results for the model in Figure 2 clearly show that when the 2D ERT crossed perpendicular to a 3D resistive structure, the resulting anomaly became similar to that of a 2D structure having the same vertical section as its orthogonal length increased. The resistivity anomaly produced became comparable with that of the homologous two-dimensional block only when the orthogonal length of the block was at least five times the side of its section.

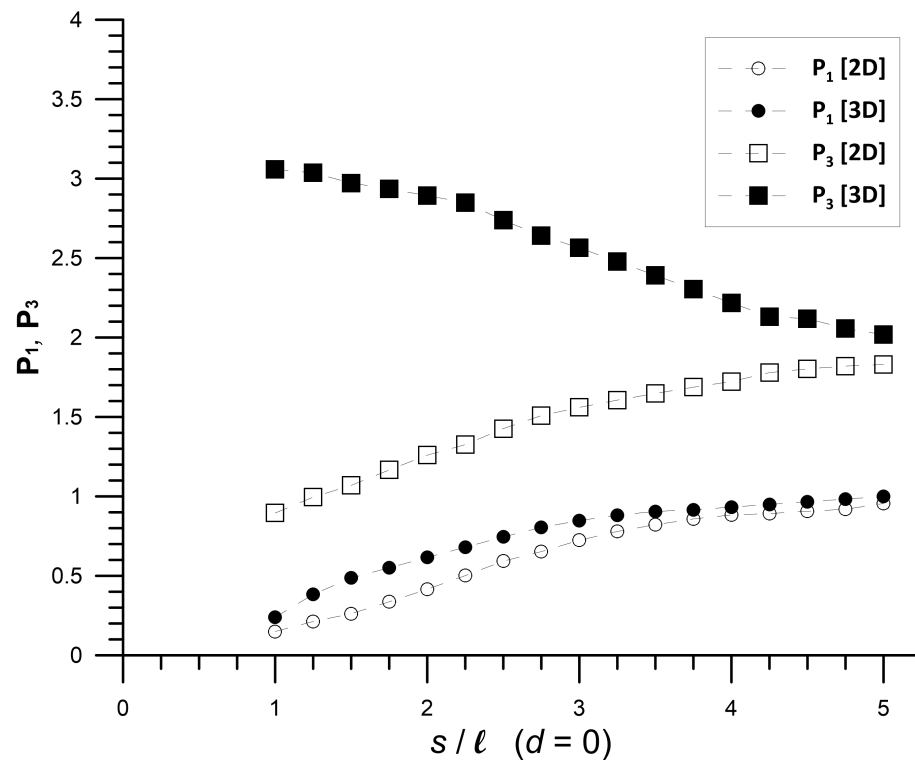


**Figure 8.** Trend of the inversion effectiveness parameters  $P_1$  and  $P_3$  referring to the 2D ERT (white squares and circles) and central sections of the 3D ERT (black squares and circles) crossing over prism-shaped models shown in Figures 2 and 3 as the  $s/l$  ratio between the orthogonal width  $s$  of the prism and the side of its square section  $l$  increased.

#### 4. Field Test

A field test was performed on a calcarenite quarry located inside the “Parco delle Cave” (Park of the Quarries) near the city of Marsala in Sicily (Figure 9). From the time of the Phoenicians until today, this area has been exploited for the extraction of Marsala Calcarenite (Middle-Inf. Pleistocene). This calcarenite is light yellow, homogeneous, well cemented, scarcely fossiliferous and present in very thick banks with calcareous granules and carbonate cement. The rock is vacuolar, highly porous and poorly fractured. The Foderà quarry (Figure 9) is currently used for tourist and cultural activities. The quarries in this area are mainly open-cast quarries, with almost regular shapes and sub-vertical excavation fronts. Most of these quarries were filled, albeit partially, with waste materials from excavation fronts of the same quarry or nearby. In the park, there are also several underground cavities, located at different depths concerning the ground level, made by excavating tunnels supported by pillars [53].

The quarry is developed in a series of tunnels and connected rooms, most of which have been subjected to underground topographic surveys with tools and software used for speleological activities. In particular, the Leica X310 laser distance measurer was used. The cavities of this quarry are almost all accessible (there are at least three entrances), and the hypogeal survey carried out allowed determining the shape and dimensions of the voids, allowing one to draw the planimetric map (Figure 10, left) and four reference sections (Figure 10, right) of the quarry.



Figure 9. The Foderà Quarry in Marsala, Sicily. View of the entrances of the main tunnels.

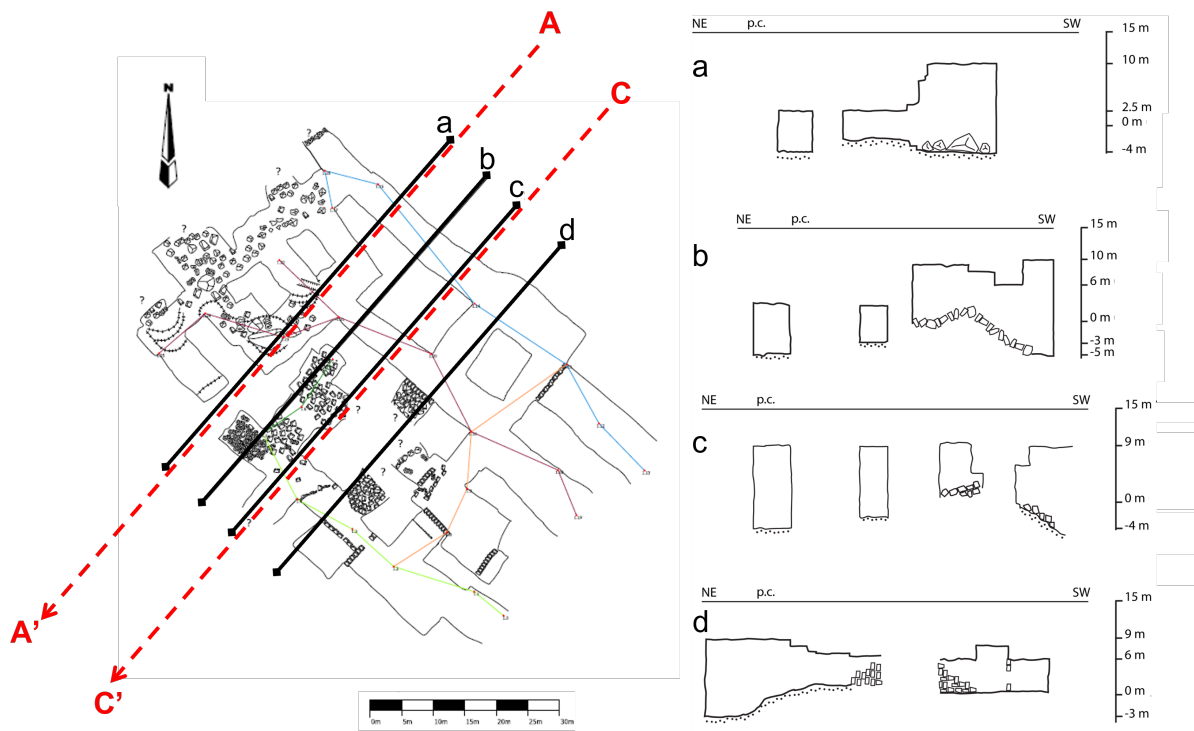


Figure 10. 3D speleological model of the Foderà Quarry: (left) planimetric map, where the thick black lines show the traces of the speleological sections (right) and the red dashed lines are the traces of the carried out electrical resistivity tomographies.

Based on the speleological survey, a simplified 3D model of subsoil resistivity was realized (Figure 11). Using RES3DMOD, we generated a discrete model of  $120\text{ m} \times 40\text{ m} \times 50\text{ m}$  with cells having horizontal dimensions equal to one meter (i.e., half the electrode spacing) and a vertical dimension increasing with the depth. The predicted data were calculated considering 60 electrodes along the  $x$  direction and 21 electrodes along the  $y$  direction. We used the same array set as for the previously discussed models (electrode spacing equal to 2 m, dipole length  $a$  ranging from 1 to 12 times the electrode spacing and dipole-dipole distance  $n$  ranging from 1 to 12 times the electrode spacing).

The modeled cave presents four main tunnels (indicated by the yellow letters *H*, *J*, *K* and *L* in Figure 11) and several short galleries and rooms (letters from *M* to *U*) that connect the main tunnels. For this model, we calculated the predicted apparent resistivity measurements relating to the same previously discussed array data set. The predicted data were inverted by RES3DINV, using the same inversion parameters as for the previous models and obtaining a data misfit equal to 3.95%.

In particular, we considered four parallel sections A–A', B–B', C–C' and D–D' in correspondence with the speleological sections (Figure 11) and extracted from the aforementioned sections of the 3D inverse model. These were compared with the 2D models obtained by separately inverting only the calculated measures relative to the parallel A–A', B–B', C–C' and D–D' lines, using RES2DINV.

Finally, of these four lines, two 2D ERTs (A–A' and C–C') were actually carried out in the field using the MAE X612-EM+ multichannel resistivity meter. Due to some subsidence of the ground, which was probably caused by the collapse of the roofs of some cavities, it was not possible to carry out lines B–B' and D–D'. The data obtained were used to make a comparison between the simulated and observed data.

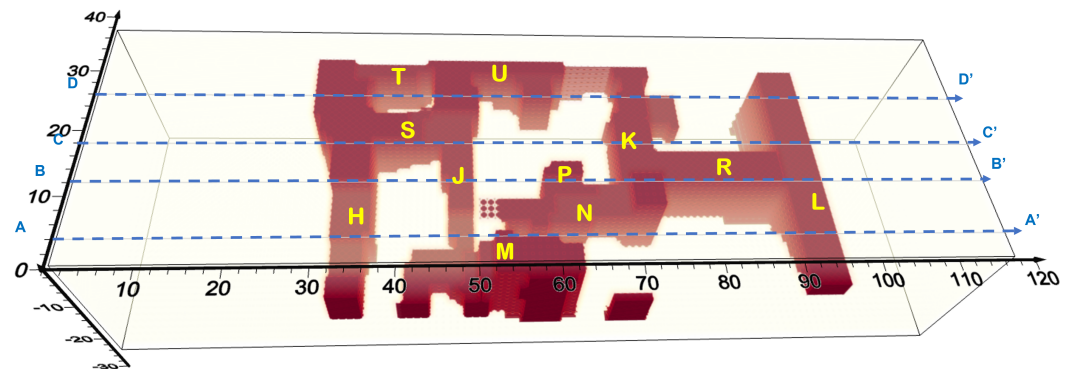


**Figure 11.** Perspective view of the simplified 3D resistivity model of the Foderà Quarry obtained by RES3DMOD™ software. The yellow letters indicate the main rooms and tunnels. The blue dashed lines indicate the traces of the simulated 2D ERTs.

Section A–A' (Figure 12a) intersects tunnels *H*, *J* and *L* and the large chamber *M* partially filled with waste material. Furthermore, tunnel *N* is present in the vicinity of the survey line (Figure 11). Overall, the section of the inverse 3D model (Figure 12b) obtained starting from the simulated data was faithful enough to the original geoelectric model. In fact, the large chamber *M* was highlighted well in terms of its shape, as the two tunnels *H* and *L* were highlighted by two smoother anomalies with lower resistivity values, while tunnel *J* was incorporated into chamber *M*.

The inverse 2D model (Figure 12c) obtained starting from the simulated data while returning a comparable data misfit value showed a lower adherence of the shapes and, above all, an anomaly in correspondence with the projection on the section of chamber *N*, which was not crossed by the section. The inverse model relating to the field measurements (Figure 12d) was quite similar to that obtained from the simulated data, except for the more superficial areas in which heterogeneous trends and higher resistivity values were noted. This can be explained by the presence of fill materials and more fractured calcarenite, which also justified the higher value of the misfit.

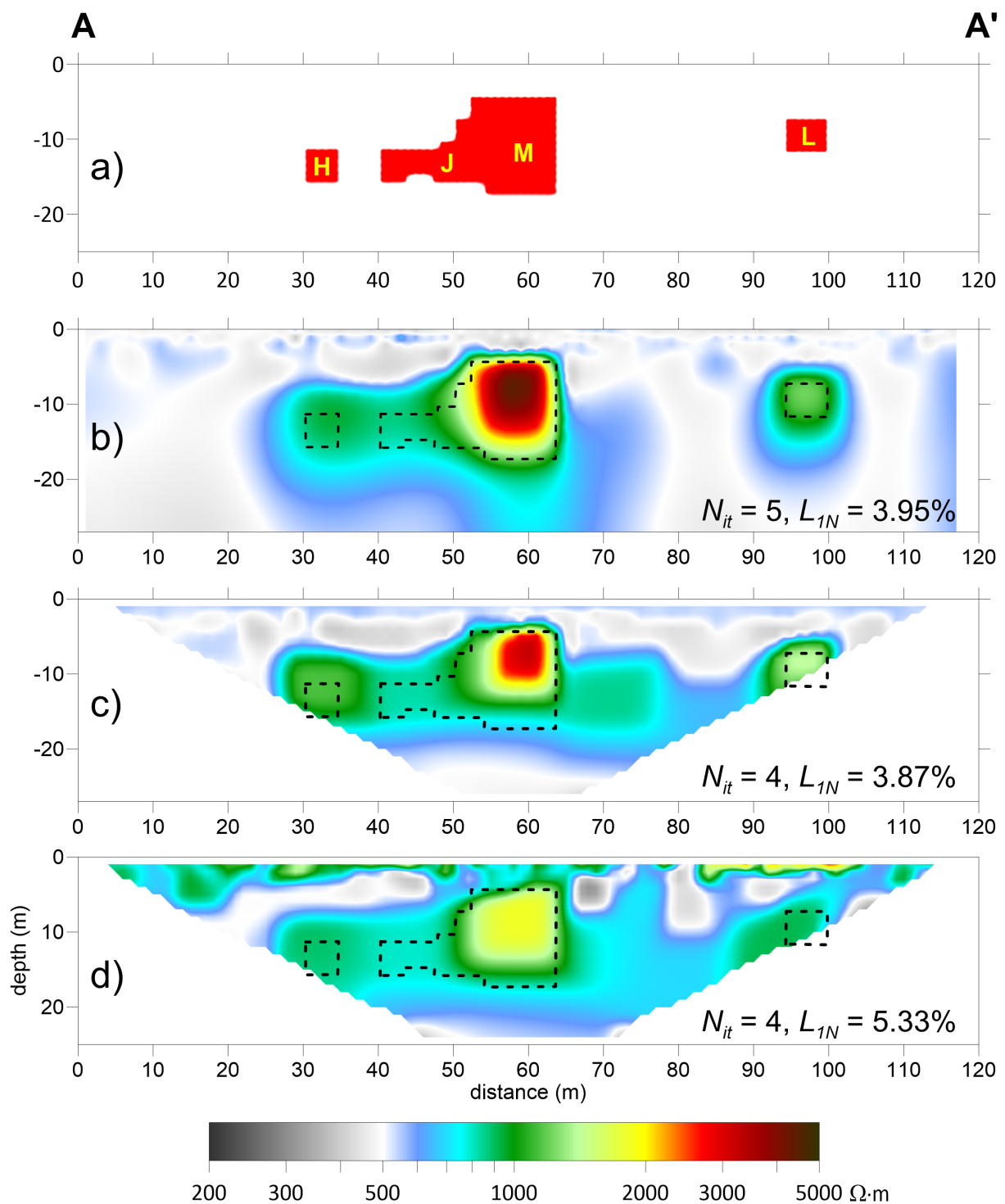


**Figure 12.** Line A–A' comparison between simulated inversion of 3D and 2D resistivity surveys and 2D inversion of field data. (a) Corresponding section of the 3D resistivity model. (b) Vertical section of the inverse model obtained by simulating a 3D survey on the geophysical model. (c) Inverse model obtained by simulating a 2D survey on the geophysical model. (d) Inverse model obtained by 2D ERT field data.

Section B–B' (Figure 13a) intersected the four main tunnels H, J, K and L, being elongated perpendicular to the section, but it was also affected by the connecting gallery N with a direction parallel to the section. Furthermore, gallery R was very close to the survey line (Figure 11).

The section of the 3D inverse model (Figure 13b) obtained from simulated data represented the geometric shapes of the intersected cavities quite well, although the anomalies showed resistivity values well below the values of the model. The 2D inverse model (Figure 13c) obtained from the simulated data, even if it showed a data misfit value similar to that of the 3D model, was less faithful and had more blunt anomalies. Furthermore, between  $x = 74$  m and  $x = 92$  m, there was an anomaly caused by gallery R not being crossed by the survey.

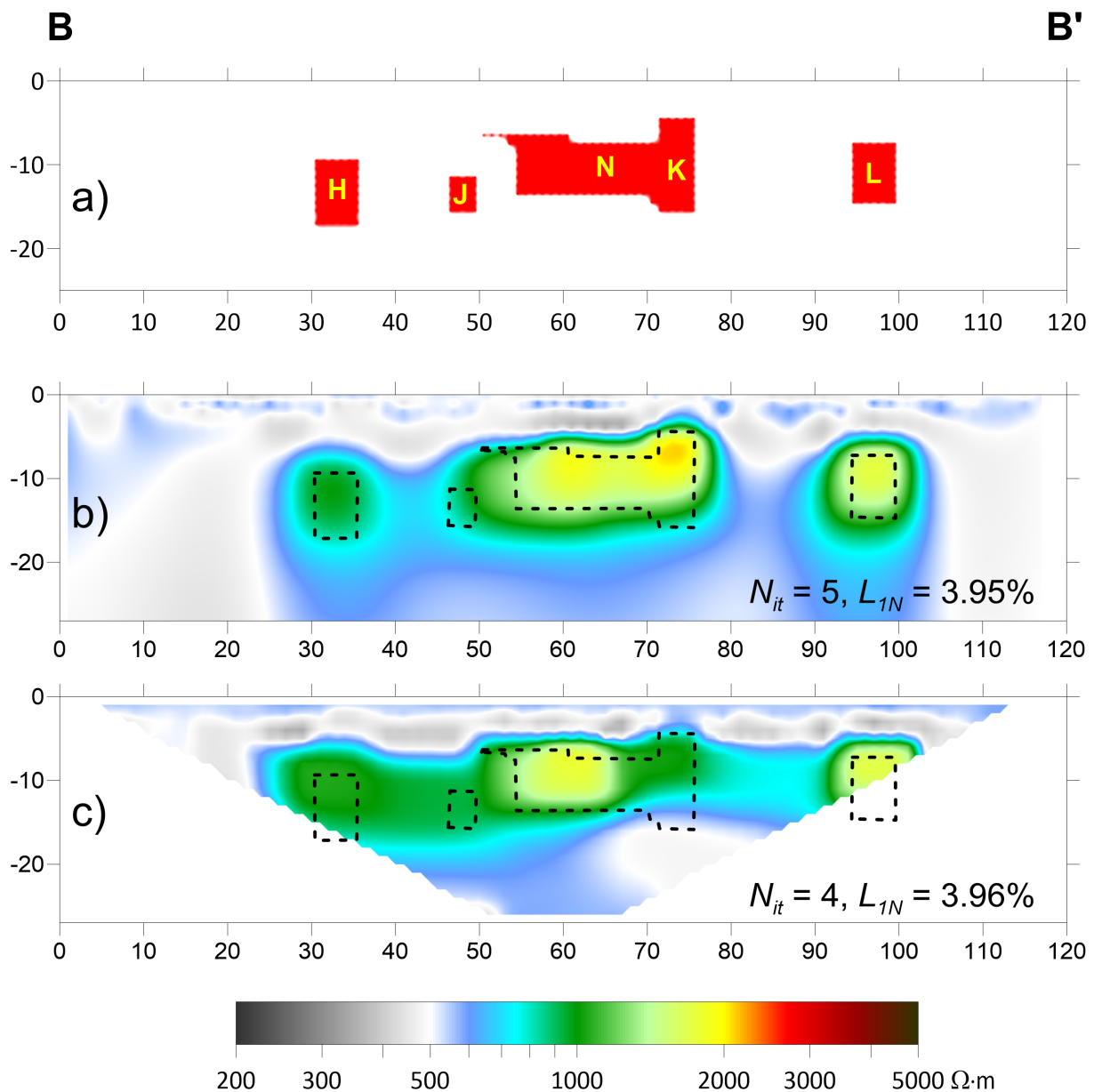


**Figure 13.** Line B–B’ comparison between simulated inversion of 3D and 2D resistivity surveys. (a) Vertical section of the 3D resistivity model. (b) Corresponding section of the inverse model obtained by simulating a 3D survey on the geophysical model. (c) Inverse model obtained by simulating a 2D survey on the geophysical model.

Section C–C’ (Figure 14a) had a very complex shape. It intersected the main tunnels H, J, K and L but also the connecting tunnel R and a small room P connected to gallery N. Furthermore, the section passed close to gallery S, which connected H with J.

The section of the 3D inverse model (Figure 14b) from the simulated data figured out the pattern of the tunnels intersected by the section very well, although the resistivity

values were not always representative of the model values. The 2D inverse model from the simulated data (Figure 14c) also had a similar data misfit in this case, was less clear and showed more smoothed patterns, especially regarding the base of the cavities. Gallery S, which was close to the line but not crossed by it, generated a clear anomaly joining H and J. The depth of investigation achieved by the field survey was lower than the simulated one because all the data with a pseudo-depth greater than 16 m were discarded, as they were too noisy. Probably due to this, the resulting misfit was greater ( $L_{1N} = 7.34\%$ ). However, the result was similar, even if it was more approximate and with greater heterogeneity, especially in the superficial part of the section.

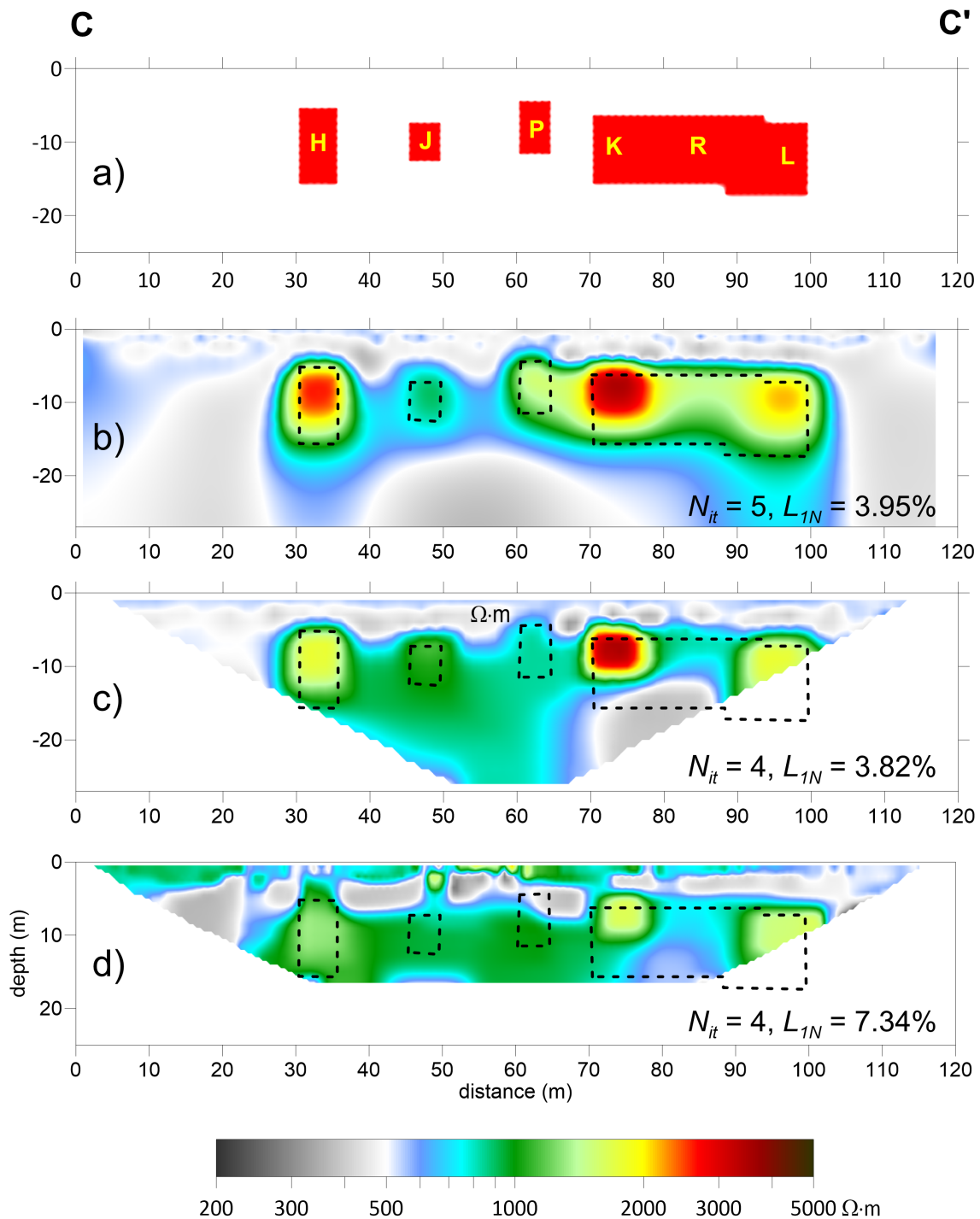
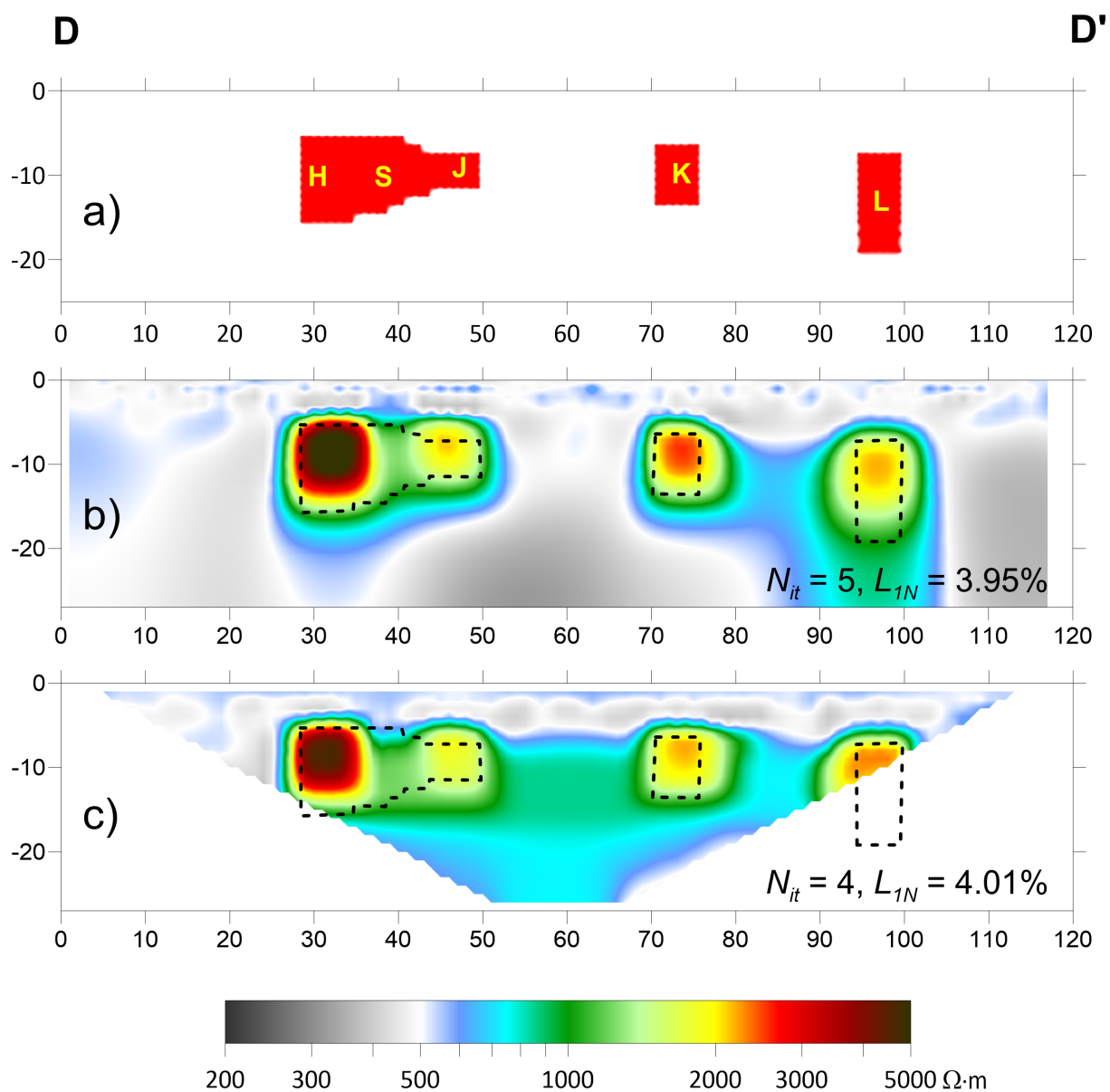


Figure 14. Line C–C' comparison between simulated inversion of 3D and 2D resistivity surveys and

2D inversion of field data. (a) Vertical section of the 3D resistivity model. (b) Corresponding section of the inverse model obtained by simulating a 3D survey on the geophysical model. (c) Inverse model obtained by simulating a 2D survey on the geophysical model. (d) Inverse model obtained by 2D ERT field data.

Finally, section D–D' intersected the main tunnels *H*, *J*, *K* and *L* and gallery *S* connecting *H* to *J*. It was also close to gallery *T*, connecting *H* with *J*, and gallery *U*, connecting *J* with *K* (Figure 15a).

In addition, in this case, although the data misfit values were comparable to each other, the section obtained from the simulated 3D inverse model (Figure 15b) was much closer to the geophysical model than the 2D inverse model (Figure 15c). Indeed, the latter clearly showed the effect of the neighboring gallery *U*. Furthermore, the base of the tunnels was not as sharply delimited.



**Figure 15.** Line D–D' comparison between simulated inversion of 3D and 2D resistivity surveys. (a) Vertical section of the 3D resistivity model. (b) Corresponding section of the inverse model obtained by simulating a 3D survey on the geophysical model. (c) Inverse model obtained by simulating a 2D survey on the geophysical model.

In summary, considering the simulated models, although the data misfit values of the 2D inverse models were comparable to those of the 3D inverse model, the latter had a greater likelihood. The sections of the 3D inverse model accurately represented the tunnels and rooms in the corresponding section, and the complexity of the shapes of the tunnels and chambers of the Foderà Quarry strongly affected the 2D inversions. These were influenced by phantom anomalies generated by the three-dimensionality of the intercepted structures and by the presence of other structures close to the investigation alignment. Moreover, the results from the 2D ERT carried out in situ were also disturbed by variations in the resistivity of the rock and by the detritus, which were not foreseen by the theoretical model.

Unfortunately, not having been able to acquire all four sections in the field prevented us from performing a 3D inversion, or, more simply, from interpolating the 2D ERTs to obtain a 3D model [54,55]. Therefore, we were limited to comparing the results relating to sections A–A' and C–C' with the 2D and 3D simulations. However, the presented results show that when the underground structures were very complex, as in this test site, the 2D ERT did not give sufficiently realistic images, even if interpolated in a 3D model.

## 5. Conclusions

A series of simulations was performed on models characterized by rectangular section resistive blocks, using the inline dipole-dipole array with a wide range of electrode spacings and dipole-dipole distances and, consequently, a high amount of apparent resistivity data. This choice allowed a very high resolution, together with a short survey time. Consequently, it enabled the comparison between 2D and 3D inversion models with similar resolutions.

The use of parameters defined in Equations (7)–(9) allowed a numerical estimation of the effects of the three-dimensionality, non-centrality of the resistive blocks and reliability of each inversion model.

The results for the synthetic tests showed that the blocks with a limited extension orthogonal to the survey line were not detected correctly by the 2D ERT. The 2D inversion of a 3D resistive block underestimated the actual resistivity value much more than the inversion of the corresponding 2D model with an unlimited perpendicular extension. Furthermore, when the 2D ERT cut an anomalous structure perpendicular to its direction of elongation, the effects of three-dimensionality decreased as the structures stretched perpendicularly. The resistivity anomaly produced was comparable with that of the homologous two-dimensional block only when the ratio between the orthogonal length of the block and the side of its section was at least equal to five.

On the other hand, when the 2D ERT was carried out near (but not above) a resistive block, this generally produced an artifact consisting of a low contrast resistivity anomaly in correspondence with the section, with an area less than that of the section.

The effects of three-dimensionality can lead to interpretative errors, such as the detection of false cavities or resistive blocks along the vertical direction or a wrong estimate of the depth and dimensions of the structures, thus causing misleading statements. These errors can be gross, especially if in the presence of very complex structures.

The results of the field test confirmed the considerations made for the simulations, showing how in the case of complex structures, the 2D inversion was even less realistic and more difficult to interpret than the 3D one. Ultimately, the simulations on the 3D model of the quarry seem to suggest that, if the data coverage is dense enough, then it might be advantageous to perform the 3D inversion rather than inverting each 2D profile individually.

**Author Contributions:** Conceptualization, R.M.; methodology, R.M.; software, R.M.; validation, R.M. and P.C.; formal analysis, R.M.; investigation, R.M. and P.C.; resources, R.M. and P.C.; data curation, R.M.; writing—original draft preparation, R.M.; writing—review and editing, R.M.; visualization, R.M.; supervision, R.M. All authors have read and agreed to the published version of the manuscript.

**Funding:** This research received no external funding.

**Institutional Review Board Statement:** Not applicable.

**Informed Consent Statement:** Not applicable.

**Data Availability Statement:** Data can be obtained upon request from the corresponding author.

**Acknowledgments:** The authors thank Marco Vattano for carrying out the speleological surveys and making the results available.

**Conflicts of Interest:** The authors declare no conflict of interest.

## References

1. Loke, M.; Chambers, J.; Rucker, D.; Kuras, O.; Wilkinson, P. Recent developments in the direct-current geoelectrical imaging method. *J. Appl. Geophys.* **2013**, *95*, 135–156. [[CrossRef](#)]
2. Chambers, J.E.; Kuras, O.; Meldrum, P.I.; Ogilvy, R.D.; Hollands, J. Electrical resistivity tomography applied to geologic, hydrogeologic, and engineering investigations at a former waste-disposal site. *Geophysics* **2006**, *71*, B231–B239.
3. Dahlin, T.; Zhou, B. Multiple-gradient array measurements for multichannel 2D resistivity imaging. *Near Surf. Geophys.* **2006**, *4*, 113–123. [[CrossRef](#)]
4. Fiandaca, G.; Martorana, R.; Messina, P.; Cosentino, P. The MYG methodology to carry out 3D electrical resistivity tomography on media covered by vulnerable surfaces of artistic value. *Il Nuovo C. B* **2010**, *125*, 711–718.
5. Johnson, T.C.; Versteeg, R.J.; Ward, A.; Day-Lewis, F.D.; Revil, A. Improved hydrogeophysical characterization and monitoring through parallel modeling and inversion of time-domain resistivity and induced-polarization data. *Geophysics* **2010**, *75*, WA27–WA41.
6. Loke, M.; Wilkinson, P.; Uhlemann, S.; Chambers, J.; Oxby, L. Computation of optimized arrays for 3-D electrical imaging surveys. *Geophys. J. Int.* **2014**, *199*, 1751–1764.
7. Martorana, R.; Capizzi, P.; D’Alessandro, A.; Luzio, D. Comparison of different sets of array configurations for multichannel 2D ERT acquisition. *J. Appl. Geophys.* **2017**, *137*, 34–48. [[CrossRef](#)]
8. Casas, A.; Cosentino, P.L.; Fiandaca, G.; Himi, M.; Macias, J.M.; Martorana, R.; Muñoz, A.; Rivero, L.; Sala, R.; Teixell, I. Non-invasive geophysical surveys in search of the Roman Temple of Augustus under the Cathedral of Tarragona (Catalonia, Spain): A case study. *Surv. Geophys.* **2018**, *39*, 1107–1124. [[CrossRef](#)]
9. Abdullah, F.M.; Loke, M.; Nawawi, M.; Abdullah, K. Assessing the reliability and performance of optimized and conventional resistivity arrays for shallow subsurface investigations. *J. Appl. Geophys.* **2018**, *155*, 237–245. [[CrossRef](#)]
10. Aizebeokhai, A.; Olayinka, A. Anomaly effects of arrays for 3d geoelectrical resistivity imaging using orthogonal or parallel 2d profiles. *Afr. J. Environ. Sci. Technol.* **2010**, *4*, 446–454.
11. Dahlin, T.; Wisén, R.; Zhang, D. 3D effects on 2D resistivity imaging—modelling and field surveying results. In Proceedings of the Near Surface 2007-13th EAGE European Meeting of Environmental and Engineering Geophysics, Istanbul, Turkey, 3–5 September 2007; European Association of Geoscientists & Engineers: Bunnik, The Netherlands, 2007.
12. Gharibi, M.; Bentley, L.R. Resolution of 3-D electrical resistivity images from inversions of 2-D orthogonal lines. *J. Environ. Eng. Geophys.* **2005**, *10*, 339–349.
13. Aizebeokhai, A.; Olayinka, A.; Singh, V.; Uhuegbu, C. Effectiveness of 3D geoelectrical resistivity imaging using parallel 2D profiles. *Curr. Sci.* **2011**, *101*, 1036–1052.
14. Inoue, K.; Nakazato, H.; Takeuchi, M.; Sugimoto, Y.; Kim, H.J.; Yoshisako, H.; Konno, M.; Shoda, D. Investigation of the line arrangement of 2D resistivity surveys for 3D inversion. *Explor. Geophys.* **2018**, *49*, 231–241.
15. Cardarelli, E.; Fischanger, F. 2D data modelling by electrical resistivity tomography for complex subsurface geology. *Geophys. Prospect.* **2006**, *54*, 121–133.
16. Dahlin, T. 2D resistivity surveying for environmental and engineering applications. *First Break.* **1996**, *14*, 275–283. [[CrossRef](#)]
17. Yang, X.; Lagmanson, M. Comparison of 2D and 3D electrical resistivity imaging methods. In Proceedings of the Symposium on the Application of Geophysics to Engineering and Environmental Problems, Seattle, DC, USA, 2–6 April 2006; Society of Exploration Geophysicists: Houston, TX, USA, 2006; pp. 585–594.
18. Sjödal, P.; Dahlin, T.; Zhou, B. 2.5 D resistivity modeling of embankment dams to assess influence from geometry and material properties. *Geophysics* **2006**, *71*, G107–G114.
19. Uhlemann, S.; Chambers, J.; Falck, W.E.; Tirado Alonso, A.; Fernández González, J.L.; Espín de Gea, A. Applying electrical resistivity tomography in ornamental stone mining: Challenges and solutions. *Minerals* **2018**, *8*, 491.
20. Dahlin, T.; Loke, M.H. Resolution of 2D Wenner resistivity imaging as assessed by numerical modelling. *J. Appl. Geophys.* **1998**, *38*, 237–249. [[CrossRef](#)]
21. Dahlin, T.; Loke, M. Quasi-3D resistivity imaging-mapping of three dimensional structures using two dimensional DC resistivity techniques. In Proceedings of the 3rd EEGS Meeting. European Association of Geoscientists & Engineers, Aarhus, Denmark, 9–11 August 1997.
22. Martorana, R.; Capizzi, P.; Carollo, A. Misinterpretation caused by 3D effects on 2d electrical resistivity tomography-tests on simple models. In Proceedings of the 24th European Meeting of Environmental and Engineering Geophysics, Porto, Portugal, 9–12 September 2018; European Association of Geoscientists & Engineers: Bunnik, The Netherlands, 2018; Volume 2018, pp. 1–5.

23. Lin, C.P.; Hung, Y.C.; Wu, P.L.; Yu, Z.H. Performance of 2-D ERT in investigation of abnormal seepage: A case study at the Hsin-Shan earth dam in Taiwan. *J. Environ. Eng. Geophys.* **2014**, *19*, 101–112. [[CrossRef](#)]
24. Cho, I.K.; Ha, I.S.; Kim, K.S.; Ahn, H.Y.; Lee, S.; Kang, H.J. 3D effects on 2D resistivity monitoring in earth-fill dams. *Near Surf. Geophys.* **2014**, *12*, 73–81.
25. Arosio, D.; Hojat, A.; Ivanov, V.; Loke, M.; Longoni, L.; Papini, M.; Tresoldi, G.; Zanzi, L. A laboratory experience to assess the 3D effects on 2D ERT monitoring of river levees. In Proceedings of the 24th European Meeting of Environmental and Engineering Geophysics Porto, Portugal, 9–12 September 2018; European Association of Geoscientists & Engineers: Bunnik, The Netherlands, 2018; Volume 2018, pp. 1–5.
26. Hojat, A.; Arosio, D.; Ivanov, V.I.; Loke, M.H.; Longoni, L.; Papini, M.; Tresoldi, G.; Zanzi, L. Quantifying seasonal 3D effects for a permanent electrical resistivity tomography monitoring system along the embankment of an irrigation canal. *Near Surf. Geophys.* **2020**, *18*, 427–443.
27. Nimmer, R.E.; Osiensky, J.L.; Binley, A.M.; Williams, B.C. Three-dimensional effects causing artifacts in two-dimensional, cross-borehole, electrical imaging. *J. Hydrol.* **2008**, *359*, 59–70. [[CrossRef](#)]
28. Feng, D.s.; Dai, Q.w.; Bo, X. Contrast between 2D inversion and 3D inversion based on 2D high-density resistivity data. *Trans. Nonferrous Met. Soc. China* **2014**, *24*, 224–232. [[CrossRef](#)]
29. Hung, Y.C.; Lin, C.P.; Lee, C.T.; Weng, K.W. 3D and boundary effects on 2D electrical resistivity tomography. *Appl. Sci.* **2019**, *9*, 2963.
30. Koefoed, O.; Geosounding Principles, 1. Resistivity Sounding Measurements. In *Methods in Geochemistry and Geophysics*; Elsevier Scientific: Amsterdam, The Netherlands, 1979; Volume 14A, 276p.
31. Dahlin, T.; Zhou, B. A numerical comparison of 2D resistivity imaging with 10 electrode arrays. *Geophys. Prospect.* **2004**, *52*, 379–398.
32. Szalai, S.; Szarka, L. On the classification of surface geoelectric arrays. *Geophys. Prospect.* **2008**, *56*, 159–175.
33. Martorana, R.; Fiandaca, G.; Casas Ponsati, A.; Cosentino, P. Comparative tests on different multi-electrode arrays using models in near-surface geophysics. *J. Geophys. Eng.* **2009**, *6*, 1–20. [[CrossRef](#)]
34. Dey, A.; Morrison, H. Resistivity modelling for arbitrarily shaped two-dimensional structures. *Geophys. Prospect.* **1979**, *27*, 106–136. [[CrossRef](#)]
35. Dey, A.; Morrison, H.F. Resistivity modeling for arbitrarily shaped three-dimensional structures. *Geophysics* **1979**, *44*, 753–780. [[CrossRef](#)]
36. Pidlisecky, A.; Haber, E.; Knight, R. RESINVM3D: A 3D resistivity inversion package. *Geophysics* **2007**, *72*, H1–H10.
37. Coggon, J. Electromagnetic and electrical modeling by the finite element method. *Geophysics* **1971**, *36*, 132–155.
38. Inman, J.R. Resistivity inversion with ridge regression. *Geophysics* **1975**, *40*, 798–817.
39. Lines, L.; Treitel, S. A review of least-squares inversion and its application to geophysical problems. *Geophys. Prospect.* **1984**, *32*, 159–186.
40. deGroot Hedlin, C.; Constable, S. Occam's inversion to generate smooth, two-dimensional models from magnetotelluric data. *Geophysics* **1990**, *55*, 1613–1624.
41. Sasaki, Y. Resolution of resistivity tomography inferred from numerical simulation. *Geophys. Prospect.* **1992**, *40*, 453–463. [[CrossRef](#)]
42. Constable, S.C.; Parker, R.L.; Constable, C.G. Occam's inversion: A practical algorithm for generating smooth models from electromagnetic sounding data. *Geophysics* **1987**, *52*, 289–300.
43. Ellis, R.; Oldenburg, D. Applied geophysical inversion. *Geophys. J. Int.* **1994**, *116*, 5–11. [[CrossRef](#)]
44. Loke, M.H.; Rucker, D.; Chambers, J.; Wilkinson, P.; Kuras, O. Electrical resistivity surveys and data interpretation. In *Encyclopedia of Solid Earth Geophysics*; Springer: Berlin/Heidelberg, Germany, 2020; pp. 1–6.
45. Farquharson, C.G.; Oldenburg, D.W. Non-linear inversion using general measures of data misfit and model structure. *Geophys. J. Int.* **1998**, *134*, 213–227.
46. Loke, M.H.; Acworth, I.; Dahlin, T. A comparison of smooth and blocky inversion methods in 2D electrical imaging surveys. *Explor. Geophys.* **2003**, *34*, 182–187. [[CrossRef](#)]
47. Loke, M. *3-D Resistivity and Ip Forward Modeling Using the Finite-Difference and Finite-Element Methods. Instruction Manual for RES3DMOD Ver. 2.14 and RES3DMODx64 Ver. 3.04*; Geotomosoft Solutions: Gelugor, Malaysia, 2017.
48. Capizzi, P.; Martorana, R.; Carollo, A.; Vattano, M. Cluster analysis for cavity detection using seismic refraction and electrical resistivity tomography. In Proceedings of the 23rd European meeting of environmental and engineering geophysics, Malmö, Sweden, 3–7 September 2017; European Association of Geoscientists & Engineers: Bunnik, The Netherlands, 2017; Volume 2017, pp. 1–5.
49. Carollo, A.; Capizzi, P.; Martorana, R. Joint interpretation of seismic refraction tomography and electrical resistivity tomography by cluster analysis to detect buried cavities. *J. Appl. Geophys.* **2020**, *178*, 104069.
50. Loke, M. *Rapid 2D Resistivity forward Modeling Using the Finite Difference and Finite Element Methods. Instruction Manual for RES2DMOD ver. 3.03*; Geotomosoft Solutions: Gelugor, Malaysia, 2016.
51. Loke, M. *Rapid 2-D Resistivity and IP Inversion Using the Least-Squares Method. Instruction Manual for RES2DINVx64 Ver. 4.07*; Geotomosoft Solutions: Gelugor, Malaysia, 2017.

52. Loke, M. *Rapid 3-D Resistivity and IP Inversion Using the Least-Squares Method. Instruction Manual for RES3DINVx64 Ver. 3.13*; Geotomosoft Solutions: Gelugor, Malaysia, 2017.
53. Bonamini, M.; Di Maggio, C.; Lollino, P.; Madonia, G.; Parise, M.; Vattano, M. Study of anthropogenic sinkholes in the Marsala area (western Sicily) through numerical analyses of instability processes in underground quarries. In Proceedings of the GeolItalia 2011, VIII Forum Italiano di Scienze della Terra. IT, Torino, Italy, 19–23 September 2011; p. 74.
54. Capizzi, P.; Martorana, R. Integration of constrained electrical and seismic tomographies to study the landslide affecting the cathedral of Agrigento. *J. Geophys. Eng.* **2014**, *11*, 045009. [[CrossRef](#)]
55. Guinea, A.; Bicknell, J.; Cox, N.; Swan, H.; Simmons, N. Characterization of legacy landfills with electrical resistivity tomography; A comparative study. *J. Appl. Geophys.* **2022**, *203*, 104716. [[CrossRef](#)]

**Disclaimer/Publisher’s Note:** The statements, opinions and data contained in all publications are solely those of the individual author(s) and contributor(s) and not of MDPI and/or the editor(s). MDPI and/or the editor(s) disclaim responsibility for any injury to people or property resulting from any ideas, methods, instructions or products referred to in the content.